electronics

MDPI

Article

Charge Transport Characteristics in Doped Organic Semiconductors Using Hall Effect

Seema Morab *, Manickam Minakshi Sundaram and Almantas Pivrikas *

College of Science, Health, Engineering and Education, Murdoch University, Perth, WA 6150, Australia; m.minakshi-sundaram@murdoch.edu.au

* Correspondence: 33649494@student.murdoch.edu.au (S.M.); a.pivrikas@murdoch.edu.au (A.P.)

Abstract: Numerical computations through the finite element method (FEM) are used to determine the impact of doping on carrier concentration and recombination between charges in time for organic semiconductor diodes having low mobility. The Hall effect is used to determine the effects of doping on the performance and reliability of organic semiconductor devices by accurately modeling these processes. In this work, the number density of charge carriers and Hall voltages are computed for n-type doped semiconductors with two different recombination processes, such as non-Langevin and Langevin-type. The findings reveal that in the Langevin system with $\beta' = 1$, the number density of charge carriers is almost five and four times lower compared with the non-Langevin system with $\beta' = 0.01$ for increasing dopant concentrations of N_{p_d} = 1 and 3, respectively. The Langevin system also had lower Hall voltages than the steady-state and non-Langevin systems for different magnetic fields with dopants, and the non-Langevin system had nearly identical Hall voltages as the steady-state case. The outcome of the current work provides insights into charge transportation mechanisms in low-mobility doped organic semiconductors with Hall effect measurements to improve device efficiency.

Keywords: carrier transport; doping; Langevin recombination; Hall effect; organic semiconductors

check for updates

Citation: Morab, S.; Sundaram, M.M.; Pivrikas, A. Charge Transport Characteristics in Doped Organic Semiconductors Using Hall Effect. *Electronics* **2024**, *13*, 4223. https://doi.org/10.3390/electronics13214223

Received: 1 October 2024
Revised: 24 October 2024
Accepted: 25 October 2024
Published: 28 October 2024

Copyright: © 2024 by the authors. Licensee MDPI, Basel, Switzerland. This article is an open access article distributed under the terms and conditions of the Creative Commons Attribution (CC BY) license (https://creativecommons.org/licenses/by/4.0/).

1. Introduction

The flexibility of organic semiconductors and devices and the more affordable large-scale roll-to-roll fabrication processes have propelled them to the forefront of the research industry in recent years. Organic light-emitting diodes (OLEDs) [1–4] and organic solar cells (OSCs) [5–7] are two examples of such devices. OLEDs have achieved significant commercial success, particularly in display applications (for example, OLED TVs and mobile phones). In-depth research has also been done on organic photovoltaics (OPVs) [8], organic field-effect transistors (OFETs) [9–14], organic thin film transistors (OTFTs) [15], and organic memories [16].

Dopants are usually added to organic semiconductors to increase their conductivity. The possibility of controlled doping was a significant component in the development of inorganic semiconductor technology. Even though most organic semiconductors are typically undoped today, the future development of effective organic-based devices will necessitate controlled and stable doping to align the Fermi levels with the transport states. Therefore, while charge carrier injection is supported, the Ohmic losses can be reduced. The fundamental idea behind doping is similar to that of inorganic semiconductors. The material is treated with electron donors or acceptors to produce more mobile charge carriers. The dopant must donate electrons to the lowest unoccupied molecular orbital (LUMO) states in order to produce n-type doping in organic materials, whereas p-type dopants must remove electrons from the highest occupied molecular orbital (HOMO) states in order to produce holes.

Strongly oxidizing gases, such as iodine or bromine, have been used to dope organic semiconductors for quite some time. High conductivities are produced by doping materials

like phthalocyanines [17–21]. However, due to their high tendency to diffuse, those dopants are too small to provide thermal stability to doped layers in bipolar devices such as p–n or p–i–n junctions. Small atoms like lithium, caesium, or strontium [22,23], as well as smaller molecules, including Lewis acids [24], have been used more frequently. A study by Parthasarathy et al. [22] that measured the Fermi level of the popular organic electron transporter bathocuproine (BCP) when doped with lithium is an excellent example of the previously mentioned effect, with lithium being used for doping and having a high tendency to diffuse. However, for practical purposes, device instability caused by diffusion is a common problem when doping with ions or extremely small molecules.

Using larger, especially aromatic molecules that function well as donors or acceptors, makes it simpler to prepare stable devices. It has been reported that there are a wide variety of materials and dopants that can be used, such as phthalocyanines that have been doped with organic acceptor molecules like tetracyano-quinodimethane (TCNQ), ortho-chloranil, or dicyano-dichloro-quinone (DDQ) [25–27]. The latter has also been employed to dope phthalocyanines [28] and oligothiophenes [29] that are covalently bound-stacked. However, the effects of these dopants were typically quite minimal. In addition, systematic research on the effects of doping on important semiconductor properties, such as the Fermi level or the charge carrier density, as well as on device performance, was generally lacking [26,29]. The physics of molecular doping has been thoroughly studied in recent years [30–32], which has resulted in the production of electrically doped transport layers that have been successfully used in both OLEDs [33–35] and OSCs [36–38].

Since charge transport in organic semiconductors is a much more complicated process, careful considerations must be made when describing the submodels and their parameters in any drift–diffusion (DD) simulation. The drift–diffusion model requires the use of the finite element method (FEM) to solve a series of equations. Previously, this DD model was used to investigate both organic and inorganic-based devices for various applications [39–41]. Additionally, it has been used in conjunction with circuit-level modeling in organic thin films to identify the low-conductive regions as a consequence of charge carrier trapping [42] and to investigate the unbalance of charge carrier mobility in organic solar cells [43].

A variety of techniques are used to study the charge transport in organic materials, including organic field-effect transistors (OFETs), space-charge-limited current (SCLC) [44], charge extraction by linearly increasing the voltage (CELIV) [45,46], time of flight (TOF) [45,47], and the Hall effect. It is possible to determine the intrinsic defect concentration, the charge carrier concentration, and the type of semiconductor (e.g., n-type or p-type) using the Hall effect method [48]. Despite the technique using the Hall effect that can ascertain holes and electron mobilities in bulk, in contrast, the above three methods described (FET, TOF, and CELIV) only account for the charge carrier mobilities in one particular direction. Choi et al. [49] reported that in high-mobility organic semiconductors, the carrier coherence factor is often close to unity, which can lead to discrepancies between Hall mobility and field-effect mobility. This discrepancy arises because Hall measurements primarily probe delocalized charge carriers, while localized carriers (which are common in organic materials) may not contribute effectively to the Hall voltage. Consequently, the Hall effect may not fully capture the transport dynamics in organic semiconductors, particularly in polycrystalline films where grain boundaries can further complicate carrier transport. Furthermore, the Hall effect is sensitive to transport mechanisms in organic semiconductors (i.e., band-like and hopping). However, this research employs the Hall effect approach to investigate the dynamic behavior of charge carriers in a two-dimensional doped organic semiconductor diode, and we report the time-dependent charge transport and recombination processes in an organic semiconductor diode with low mobility in the presence of doping.

A suitable semiconductor composite or device should have high efficiency and low energy consumption. It should also be durable and cost-effective. Furthermore, it should be compatible with existing technologies. In addition, it should be environmentally friendly and sustainable. Finally, it should be easily scalable for mass production. In order to pre-

dict charge transport in low-mobility organic semiconductors in the presence of magnetic fields and understand their potential applications in electronic devices, two-dimensional modeling techniques can be employed to simulate charge carrier behavior. This is because one-dimensional device models cannot show the separation of charge carriers in the presence of both electric and magnetic fields, generating another electric field component perpendicular to the direction of current flow leading to the Hall voltage. This perpendicular electric field can significantly impact the overall charge transport characteristics of the semiconductor material. The Hall voltage is a measurable quantity that can be used to determine important material properties such as carrier concentration and mobility in the semiconductor. By utilizing two-dimensional modeling techniques, researchers can gain a more comprehensive understanding of how magnetic fields influence charge carrier behavior in low-mobility organic semiconductors, ultimately informing the design and optimization of electronic devices to be more efficient and reliable. This can lead to the development of new technologies with improved performance and functionality. A thorough investigation and improved charge transport optimization in semiconductors significantly improve the device's performance. New insights into charge transport in doped organic semiconductors will be presented in the current work.

The current project is set up as follows: Using the finite element method (FEM) and a drift–diffusion–recombination solver, Section 2 creates a two-dimensional semiconductor model with dopants. The parameter settings necessary for the simulations are also provided in this section. The results are presented in Section 3, which also compares the Langevin and non-Langevin systems and highlights all important figures of merit like Hall voltages and number density of charge carriers within the device. Final conclusions are made in Section 4.

2. Methodology

2.1. Device Modelling Using Numerical Methods

A one-dimensional drift–diffusion–recombination solver [50–55] was used to develop the organic semiconductor device model. To evaluate the number density of charge carriers with Hall effect parameters under the influence of an external magnetic field, device geometry was expanded from one dimension to two dimensions. Briefly, Poisson's equation for the electric field and the continuity equations for electrons and holes [50–52,56,57] were solved simultaneously. Two-dimensional geometry was used to model the Hall effect, with application of Poisson and continuity equations to charges. In this model, dopants were added to obtain either n-type, p-type, or compensation-doped semiconductors. These dopants increase the number of charge carriers in the semiconductor and modify its optical, electrical, and structural properties. In the case of compensation doping, an equal number of donors and acceptors are present within the same semiconductor. Usually, donors are n-type, and acceptors are p-type. To obtain dimensionless units, all quantities were normalized. The physical units like length, voltage, and time were chosen as reference scales to achieve this. For nondimensionalization, a technique similar to Juška et al. [58,59] was employed. A prime symbol was used to represent the dimensionless quantities. The applied voltage was normalized to reference voltage given by $\frac{U_{App}}{U_{Ref}} = U'$, where $U_{Ref} = 1$. Then the normalisation of electric field was $\frac{E\,d}{U_{Ref}} = E'$. Position coordinates were normalized as $\frac{x}{d} = x'$ and $\frac{y}{d} = y'$, while time coordinate was normalized as $\frac{t}{t_{tr}} = t'$, where transit time of charge carriers was represented by t_{tr} and thickness of the semiconductor was represented by 'd'. Transit time t_{tr} refers to the duration it takes for charge carriers, such as electrons or holes, to travel through a semiconductor device under the influence of an electric field. The normalized faster charge carrier mobility was $\mu'_{(Fast)} = 1$. The charge scale was normalized as $\frac{Q}{C\,U_{Ref}} = Q'$. Therefore, the normalisation of number density of electrons and holes to charge scale was $\frac{Sden}{C U_{Ref}} = n'$ and $\frac{Sdep}{C U_{Ref}} = p'$, where semiconductor's surface area was represented by 'S'. Similarly, normalisation of number density of dopant electrons

and dopant holes to charge scale was $\frac{Sden_d}{CU_{Ref}} = n'_d$ and $\frac{Sdep_d}{CU_{Ref}} = p'_d$. The temperature was normalized as $\frac{T k_B}{eU_{Ref}} = T'$ and normalized conduction current density was $\frac{t_{tr}}{CU_{Ref}} jS = j'$. The magnetic force was normalized to electric force as $\frac{F_{Mag}}{F_{Ele}} = \frac{F_{Mag}}{e\left(\frac{U_{Ref}}{d}\right)} = F'$, and the normalized magnetic flux density was given by $\frac{d^2}{t_{tr}\, U_{Ref}} B = B'$. The normalisation of recombination rate was $\frac{\beta}{\beta_L} = \beta'$, where β and β_L represent recombination rate and Langevin rate, respectively. In the presence of dopants, equations that are normalized for a semiconductor device with two dimensions are given by

$$\mathrm{j'_{n+n_d(x)}}(\mathrm{x'},\mathrm{t'}) = \mathrm{j'_n}(\mathrm{x'},\mathrm{t'}) + \mathrm{j'_{n_d}}(\mathrm{x'},\mathrm{t'}) \tag{1}$$

$$\mathrm{j'_{n+n_d(y)}}(\mathrm{y'},\mathrm{t'}) = \mathrm{j'_n}(\mathrm{y'},\mathrm{t'}) + \mathrm{j'_{n_d}}(\mathrm{y'},\mathrm{t'}) \tag{2}$$

$$\mathrm{j'_{p+p_d(x)}}(\mathrm{x'},\mathrm{t'}) = \mathrm{j'_p}(\mathrm{x'},\mathrm{t'}) + \mathrm{j'_{p_d}}(\mathrm{x'},\mathrm{t'}) \tag{3}$$

$$\mathrm{j'_{p+p_d(y)}}(\mathrm{y'},\mathrm{t'}) = \mathrm{j'_p}(\mathrm{y'},\mathrm{t'}) + \mathrm{j'_{p_d}}(\mathrm{y'},\mathrm{t'}) \tag{4}$$

$$\frac{\partial(\mathrm{n'}+\mathrm{n'_d})}{\partial \mathrm{t'}} - \frac{\partial \mathrm{j'_{n+n_d(x)}}(\mathrm{x'},\mathrm{t'})}{\partial \mathrm{x'}} = -\mathrm{r'}(\mathrm{x'},\mathrm{t'}) \tag{5}$$

$$\frac{\partial(\mathrm{n'}+\mathrm{n'_d})}{\partial \mathrm{t'}} - \frac{\partial \mathrm{j'_{n+n_d(y)}}(\mathrm{y'},\mathrm{t'})}{\partial \mathrm{y'}} = -\mathrm{r'}(\mathrm{y'},\mathrm{t'}) \tag{6}$$

$$\frac{\partial(\mathrm{p'}+\mathrm{p'_d})}{\partial \mathrm{t'}} + \frac{\partial \mathrm{j'_{p+p_d(x)}}(\mathrm{x'},\mathrm{t'})}{\partial \mathrm{x'}} = -\mathrm{r'}(\mathrm{x'},\mathrm{t'}) \tag{7}$$

$$\frac{\partial(\mathrm{p'}+\mathrm{p'_d})}{\partial \mathrm{t'}} + \frac{\partial \mathrm{j'_{p+p_d(y)}}(\mathrm{y'},\mathrm{t'})}{\partial \mathrm{y'}} = -\mathrm{r'}(\mathrm{y'},\mathrm{t'}) \tag{8}$$

$$\frac{\partial^2 \mathrm{V'}}{\partial(\mathrm{x'})^2} = (\mathrm{n'}+\mathrm{n'_d}) - (\mathrm{p'}+\mathrm{p'_d}) \tag{9}$$

$$\frac{\partial^2 \mathrm{V'}}{\partial(\mathrm{y'})^2} = (\mathrm{n'}+\mathrm{n'_d}) - (\mathrm{p'}+\mathrm{p'_d}) \tag{10}$$

The terms $\mathrm{j'_n}, \mathrm{j'_{n_d}}, \mathrm{j'_p}$ and $\mathrm{j'_{p_d}}$ in Equations (1)–(4) represent conduction current density of electrons, dopant electrons, holes, and dopant holes, respectively. The electron current density in x-direction was given by $j'_n(x',t') = n'(x',t')E'(x',t')\mu'_{\mathrm{n}} + T'\mu'_{\mathrm{n}}\frac{\partial \mathrm{n'}}{\partial \mathrm{x'}}$ and current density for dopant electrons in x direction was $j'_{n_d}(x',t') = n'_d(x',t')E'(x',t')\mu'_{\mathrm{n_d}} + T'\mu'_{\mathrm{n_d}}\frac{\partial n'_d}{\partial x'}$.

For y-direction, normalized force was used within the conduction current density equations such that $j'_n(y',t') = n'(y',t')F'(y',t')\mu'_{\mathrm{n}} + T'\mu'_{\mathrm{n}}\frac{\partial \mathrm{n'}}{\partial \mathrm{y'}}$ and $j'_{n_d}(y',t') = n'_d(y',t')\,F'(y',t')\mu'_{\mathrm{n_d}} + T'\mu'_{\mathrm{n_d}}\frac{\partial n'_d}{\partial y'}$. Where $F'_n(y',t') = B'(-z',t')\;E'(x',t')\mu'_{\mathrm{n}}$ and $F'_{n_d}(y',t') = B'(-z',t')\;E'(x',t')\mu'_{\mathrm{n_d}}$.

Similar equations are defined for current density of holes and dopant holes in both x and y directions with negative sign in diffusion term, for example $j'_p(x',t') = p'(x',t')E'(x',t')\mu'_{\mathrm{p}} - T'\mu'_{\mathrm{p}}\frac{\partial p'}{\partial x'}$. The terms $\mathrm{n'}, \mathrm{n'_d}, \mathrm{p'}$ and $\mathrm{p'_d}$ in Equations (5)–(10) represent number densities of electrons, dopant electrons, holes, and dopant holes, respectively.

For instance, the calculated structure of the model employes normalized quantities to obtain normalized conduction current density, normalized continuity, and Poisson equations in x-direction, respectively, as shown below.

$$j_n(x,t) = e\mu_n E(x,t)n(x,t) + \mu_n k_B T\frac{\partial n}{\partial x} \tag{11}$$

$$j'\left[\frac{C\,U_{ref}}{t_{tr}\,S}\right] = e\left[\mu'\frac{d^2}{U_{ref}\,t_{tr}}\right]\left[E'\frac{U_{ref}}{d}\right]\left[\mathrm{n'}\frac{\mathrm{CU_{ref}}}{\mathrm{eSd}}\right] + \left[\mu'\frac{d^2}{U_{ref}\,t_{tr}}\right](k_B)\left[T'\frac{eU_{ref}}{k_B}\right]\frac{\partial}{\partial(x'd)}\left[n'\frac{CU_{ref}}{eSd}\right]$$

$$j'_n(x',t') = \mu'_n E'(x',t') n'(x',t') + \mu'_n T' \frac{\partial n'}{\partial x'} \tag{12}$$

$$\frac{\partial n}{\partial t} - \frac{1}{e}\frac{\partial j_n}{\partial x} = -r(x,t) \tag{13}$$

$$\frac{\partial}{\partial(t'\,t_{tr})}\left[n'\frac{CU_{ref}}{eSd}\right] - \frac{1}{e}\,\frac{\partial}{\partial(x'\,d)}\,\left[j'\,\frac{C\,U_{ref}}{t_{tr}\,S}\right] = -\left[r'\frac{CU_{ref}}{eSd\,t_{tr}}\right]$$

$$\left[\frac{CU_{ref}}{eSd\,t_{tr}}\right]\left[\frac{\partial n'}{\partial t'} - \frac{\partial j'_n}{\partial x'}\right] = \left[\frac{CU_{ref}}{eSd\,t_{tr}}\right]\,\left[-r'(x',t')\right]$$

$$\frac{\partial n'}{\partial t'} - \frac{\partial j'_n}{\partial x'} = -r'(x',t') \tag{14}$$

$$\frac{\partial^2 V}{\partial x^2} = \frac{e(n-p)}{\epsilon_0 \epsilon_r} \tag{15}$$

$$\frac{\partial^2(V'\;V_{ref})}{\partial(x'd)^2} = \frac{e}{\epsilon_0\epsilon_r}\left[n'\,\frac{\epsilon_0\epsilon_r\,U_{ref}}{ed^2} - p'\,\frac{\epsilon_0\epsilon_r\,U_{ref}}{ed^2}\right]$$

$$\frac{U_{ref}}{d^2}\,\frac{\partial^2 V'}{\partial(x')^2} = \frac{e}{\epsilon_0\epsilon_r}\left[\frac{\epsilon_0\epsilon_r\,U_{ref}}{ed^2}\right](n'-p') \quad (where\ V_{ref} = U_{ref})$$

$$\frac{\partial^2 V'}{\partial(x')^2} = n' - p' \tag{16}$$

These above normalized equations can be calculated similarly for y-direction and also calculated similarly for dopant electrons (n_d) and dopant holes (p_d), and finally these equations are added to obtain Equations (1)–(10).

On each injecting electrode, $j'_n(x',t') = n'(x',t')E'(x',t')\mu'_n$ describing drift current for electrons (with similar equation for holes) defines the fluxes that represent the boundary conditions for carrier transport. Using the Dirichlet boundary conditions, charge carriers were injected through injecting electrodes while a voltage of $V' = 1$ was applied under forward bias. The boundary conditions for Poisson equation were $U'(x' = 0, t') = 0$ and $U'(x' = 1, t') = V'$, with applied electric field defined as $E' = -\frac{\partial V'}{\partial x'}$. The number density of charge carriers (p', n') with their respective derivatives in time ($\frac{\partial p'}{\partial t'}$, $\frac{\partial n'}{\partial t'}$) had initial values set to zero.

2.2. Simulation Settings

A two-dimensional geometry for the device was employed in the simulations, and the Dirichlet boundary conditions set the initial electron and hole densities at each injecting electrode to 100, and transient injection was employed at injecting electrodes. Figure 1 shows two-dimensional structure of the semiconductor device where the electrons (n) are injected at x = 0 and holes (p) are injected at x = 1 at the same time. The recombination rates in x and y directions were given by $r'(x',t') = r'(y',t') = n'p'(\mu'_p + \mu'_n)\beta'$. Because dopants cannot recombine with each other or with injected charge carriers, the recombination rates $r'(x',t')$ and $r'(y',t')$ become zero. Therefore, the Langevin and non-Langevin recombination is possible only between injected charge carriers. In the simulation settings, dopants are made available within the two-dimension semiconductor domain, and these dopants do not have to recombine with each other. Therefore, the recombination rates are kept to 'zero' for both "continuity equations of dopant electrons" and "continuity equations of dopant holes". Hence, allowing the recombination process to take place only between the electrons and holes that are injected through electrodes. Also, the faster carrier mobility is $\mu' = 1$ and slower carrier mobility $\mu' < 1$. Non-Langevin materials had the recombination rate $\beta' < 1$, and Langevin materials had recombination rate $\beta' = 1$ [60,61]. Balanced mobility ratio of charge carriers was represented by $\mu_{faster}/\mu_{slower} = 1$. However, the mobilities of dopant electrons (μ'_{n_d}) and dopant holes (μ'_{p_d}) must be less than 1. The dopant concentration in the domain was set to 1 and 3 [30,62–64]. In the (−z) direction, the magnetic field was applied to the device with values ranging between zero and one [65], and temperature was kept equal to 1×10^{-2}.

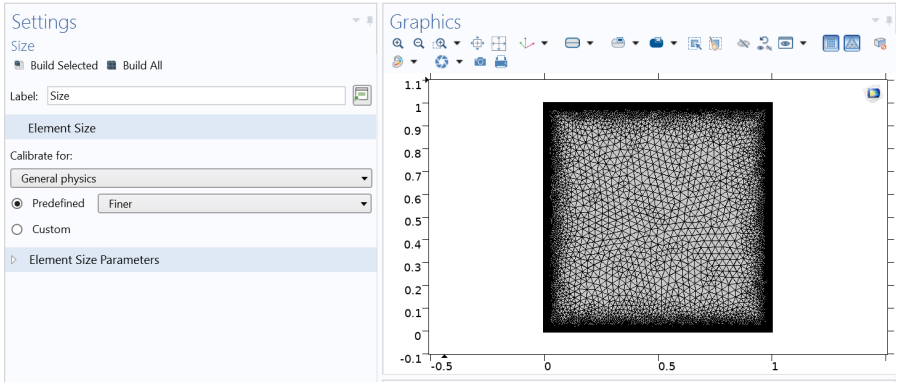


Figure 1. Two-dimension structure with meshing techniques for Hall effect. The electrons (n) injected at x = 0 and holes (p) injected at x = 1 at the same time. The left panel shows element size calibrated for general physics with 'finer' mesh size. The right panel shows free triangular mesh with all boundaries selected for the geometry.

The finite element method (FEM) was used to simulate the model's normalized equations, which were implemented for computation in COMSOL Multiphysics. A quadratic element-order Lagrange shape function with the spatial frame was used for discretization. The continuity and Poisson equations were solved using the "general form partial differential equation (PDE)" in time. The free triangular mesh with a "finer" mesh size was used, and the number of mesh elements was kept equal to 500 for the stability and convergence of the results.

3. Results and Discussion

Electrons and holes were injected at the same time from the left and right sides into the two-dimensional semiconductor device. This is because simultaneous injection allows both electrons and holes to enter into the bulk of the semiconductor device more efficiently and also allows an external magnetic field to act on these charges at the same time to generate the Hall voltage. Moreover, the dopants were added to the device, which moved throughout the bulk of the semiconductor device. The negative and positive dopants for electrons and holes were denoted by n_d and p_d, respectively.

There were three types of doping in the semiconductor model: n-type, p-type, and compensation doping. For n-type doping, the concentration of positive dopants (N_{p_d}) was active, and this was given a value of 1 (or 3), whereas the concentration of negative dopants (N_{n_d}) was set to zero. The positive (holes) dopant mobility μ_{p_d} was equal to 1×10^{-3}, and the negative (electrons) dopant mobility μ_{n_d} was zero. The initial values for n_d = 0 and $p_d = N_{p_d}$ = 1 (or 3) were specified within their respective PDE nodes.

For p-type doping, the positive dopant concentration (N_{p_d}) was set to zero, whereas the negative dopant concentration (N_{n_d}) was active and was represented by the value 1 (or 3). μ_{p_d}, the positive (holes) dopant mobility, was zero, and μ_{n_d}, the negative (electrons) dopant mobility, was 1×10^{-3}. The initial values for $n_d = N_{n_d}$ = 1 (or 3) and p_d = 0 were specified within their respective PDE nodes.

In the case of compensation doping, both the positive (N_{p_d}) and negative (N_{n_d}) dopant concentrations were active, and this value was given by 1 (or 3). Furthermore, both the positive (holes) dopant mobility μ_{p_d} and the negative (electrons) dopant mobility μ_{n_d} were equal to 1×10^{-3}. The initial values for $n_d = N_{n_d}$ = 1 (or 3) and $p_d = N_{p_d}$ = 1 (or 3) were defined within their respective PDE nodes. However, p-type and compensation doping results were not discussed in this paper since the compensation doping had an equal number of dopant concentrations and the number density of charge carriers would increase slightly depending upon the dopant concentration added to the semiconductor. Furthermore, the results of p-type doping were similar to those of n-type doping but in reverse, with the majority of charge carriers acting as holes and the minority acting as electrons.

For different recombination coefficients β', numerical simulations were run to predict the number density of charge carriers and the Hall voltage for an n-type doped semiconductor with respect to the magnetic field $B'(z)$, position coordinate x' or y', and time t'. Therefore, the results for n-type doping within the semiconductor device are discussed below in the two sections (Sections 3.1 and 3.2).

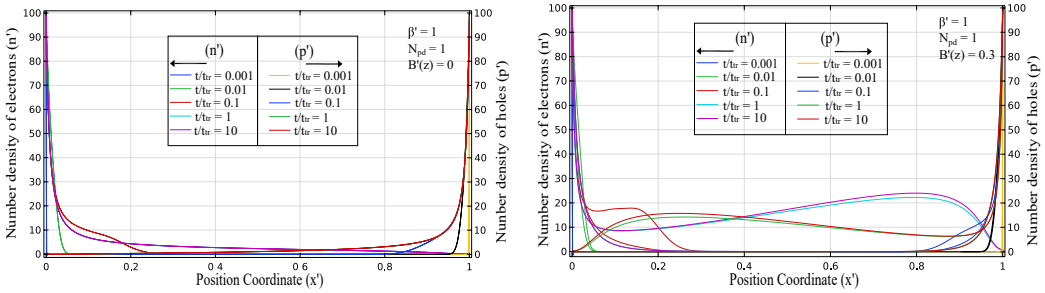
3.1. Impact of n-Type Doping on Number Density of Carriers

Figures 2–5 illustrate the normalized number densities of holes (p') and electrons (n') varying with respect to x', which is a position coordinate for an n-type doped semiconductor with different magnetic fields at varying time scales. The dopant concentrations added to the semiconductor were 1 and 3. The left y-axis represents the number density of electrons, and the right y-axis represents the number density of holes. Impact of Lorentz force on number density of charge carriers has been examined for times $\frac{t}{t_{tr}}$ = 0.001, 0.01, 0.1, 1, and 10 in both Langevin and non-Langevin systems by changing magnetic field values between zero and one.

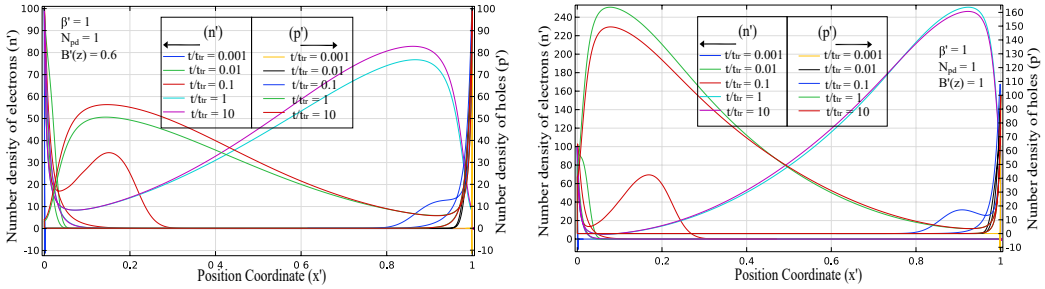
Figure 2a demonstrates that the number density of electrons and holes decreased with increasing time from $\frac{t}{t_{tr}} = 0.001$ to 10 for zero magnetic field at Langevin recombination rate $\beta' = 1$. In Figure 2b–d, as mentioned earlier, the left y-axis represents the number density of electrons, and the right y-axis represents the number density of holes. The rise of (p) at x = 1 is in fact the increase in the number density of electrons (n). This is because the concentration of electrons is greater than that of holes in an n-type semiconductor. In these figures, the number density of electrons from left at x = 0 decreases initially with increasing time from $\frac{t}{t_{tr}}$ = 0.001 and 0.01, then starts increasing for time 0.1, 1, and 10 and reaches maximum value on opposite side (to right y-axis) at x = 1. Similarly, the number density of holes from right at x = 1 decreases initially with increasing time from $\frac{t}{t_{tr}}$ = 0.001 and 0.01, then starts increasing for time 0.1, 1, and 10 and reaches maximum value on opposite side (to left y-axis) at x = 0. As shown in Figure 2b–d, for times 1 and 10, a rise in the number density of carriers was observed with higher magnetic field values between 0.3 and 1 and a fall was observed with a rising time of $\frac{t}{t_{tr}} = 0.001$ and 0.01, further at time $\frac{t}{t_{tr}} = 0.1$, an irregularity was displayed. For $B'(z)$ = 0.3, 0.6, and 1, the corresponding electron concentration increases were greater than 20, 80, and 240, respectively, and the corresponding hole concentration increases were greater than 10, 50, and 160, respectively. Because electrons constitute the majority of charge carriers in an n-type semiconductor, the electron concentration is increased relative to the hole concentration.

Figure 3 shows that while keeping $\beta' = 0.01$, which is non-Langevin recombination, and rising time from 0.001 to 0.1, the number density of electrons and holes initially decreased. However, with a further rise in time from 1 to 10 and magnetic field values between 0 and 1, the number density of charges advanced to the highest values, approximately 100 and 100, 140 and 130, 360 and 320, and 1400 and 1300. Therefore, with rising magnetic fields and times, there was a rise in the number density of charges. The concentration of electrons is greater than that of holes in an n-type semiconductor because electrons make the majority of the charge carriers in this type of semiconductor.

Figures 2 and 3 depict that, compared with the non-Langevin system, the Langevin system had a lower number density of charge carrier because of a higher recombination rate with varying magnetic fields. Therefore, results showed that the maximum electron concentration for an n-type doped semiconductor with dopant concentration of $N_{p_d} = 1$ with $\beta' = 0.01$ for a non-Langevin system was approximately five times higher compared with that of the Langevin system.

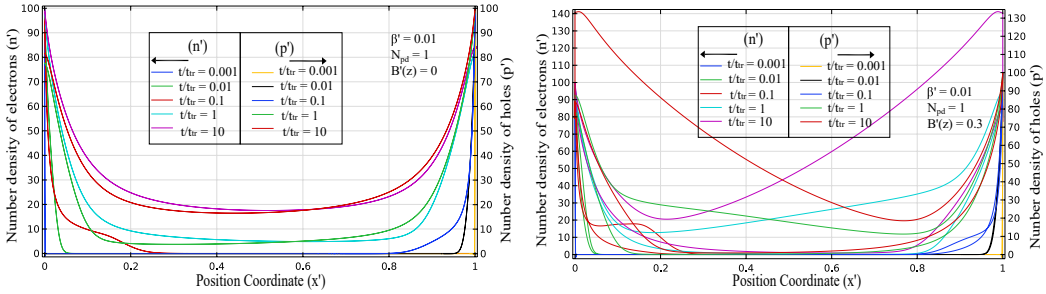


(**a**) For $\beta' = 1$, $N_{p_d} = 1$ and $B'(z) = 0$ (**b**) For $\beta' = 1$, $N_{p_d} = 1$ and $B'(z) = 0.3$

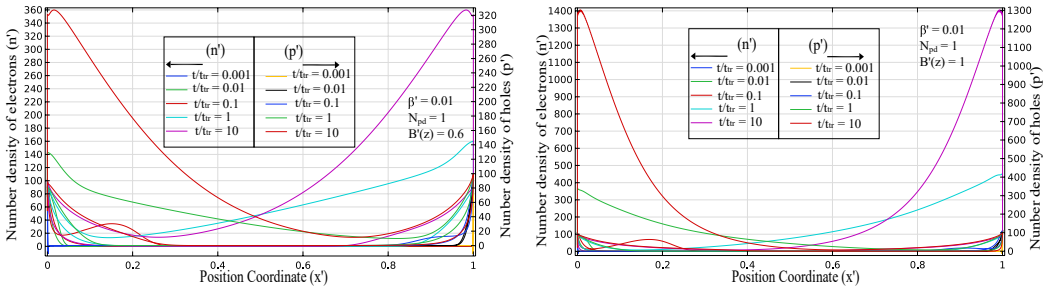


(**c**) For $\beta' = 1$, $N_{p_d} = 1$ and $B'(z) = 0.6$ (**d**) For $\beta' = 1$, $N_{p_d} = 1$ and $B'(z) = 1$

Figure 2. Number density of electrons and holes varying with respect to position coordinate, magnetic field, and time for an n-type doped semiconductor with a dopant concentration of $N_{p_d} = 1$ in Langevin system $\beta' = 1$.



(**a**) For $\beta' = 0.01$, $N_{p_d} = 1$ and $B'(z) = 0$ (**b**) For $\beta' = 0.01$, $N_{p_d} = 1$ and $B'(z) = 0.3$

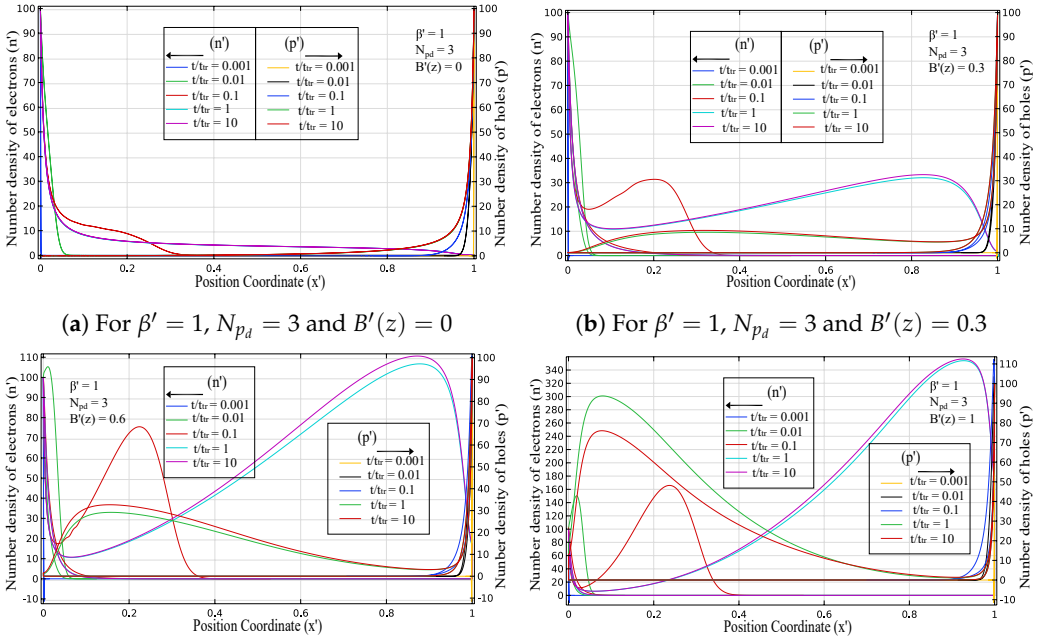


(**c**) For $\beta' = 0.01$, $N_{p_d} = 1$ and $B'(z) = 0.6$ (**d**) For $\beta' = 0.01$, $N_{p_d} = 1$ and $B'(z) = 1$

Figure 3. Number density of electrons and holes varying with respect to position coordinate, magnetic field, and time for an n-type doped semiconductor with a dopant concentration of $N_{p_d} = 1$ in non-Langevin system $\beta' = 0.01$.

Figure 4a illustrates that for zero magnetic field with Langevin recombination between charge carriers, the number density of electrons and holes reduced as the time increased from $\frac{t}{t_{tr}} = 0.001$ to 10. According to Figure 4b–d, for times $\frac{t}{t_{tr}} = 1$ and 10, the concentrations increased with the rising magnetic fields between 0.3 and 1, but decreased with increasing

time of $\frac{t}{t_{tr}}$ = 0.001 and 0.01. The corresponding increases in electron concentration were higher than 30, 110, and 340 for $B'(z)$ = 0.3, 0.6, and 1, respectively, and the corresponding increases in hole concentration were higher than 10, 30, and 90, respectively. Since in an n-type semiconductor, the majority of charge carriers are electrons, the electron concentration is higher than the hole concentration. An irregularity at time $\frac{t}{t_{tr}}$ = 0.1 was observed for electron concentration. This irregularity increased as the dopant concentration increased from 1 to 3.



(**a**) For $\beta' = 1$, $N_{p_d} = 3$ and $B'(z) = 0$

(**b**) For $\beta' = 1$, $N_{p_d} = 3$ and $B'(z) = 0.3$

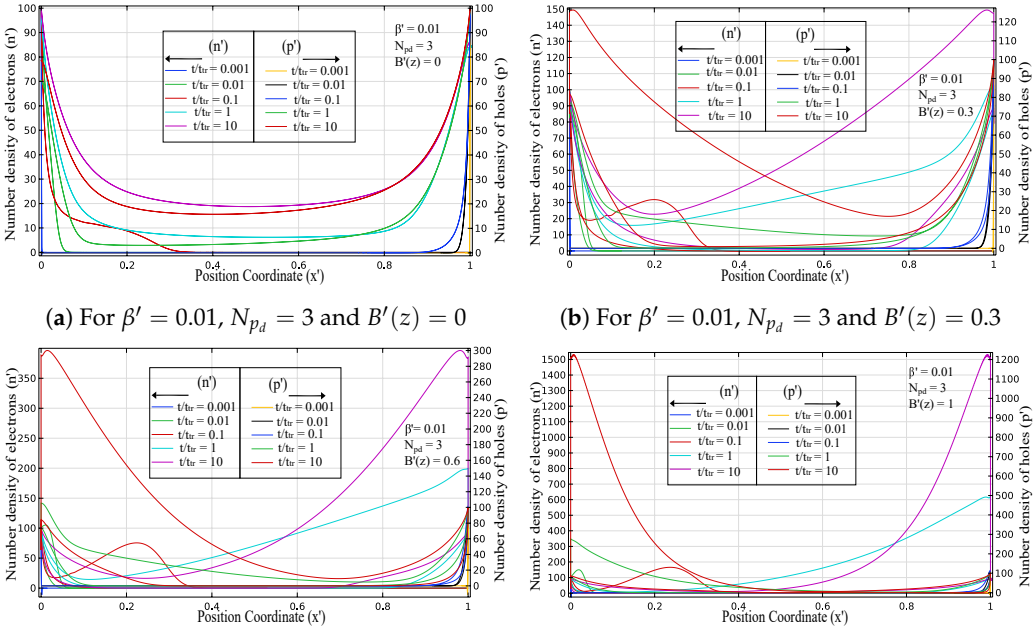
(**c**) For $\beta' = 1$, $N_{p_d} = 3$ and $B'(z) = 0.6$

(**d**) For $\beta' = 1$, $N_{p_d} = 3$ and $B'(z) = 1$

Figure 4. Number density of electrons and holes varying with respect to position coordinate, magnetic field and in time for an n-type doped semiconductor with a dopant concentration of $N_{p_d} = 3$ in Langevin system $\beta' = 1$.

Analogous to Figure 3, Figure 5 shows that number densities of electrons and holes initially decreased for $\beta' = 0.01$, which is a non-Langevin recombination case with rising time from 0.001 to 0.1. However, with a further rise in time from 1 to 10 and magnetic field values between 0 and 1, the number density of charge carriers advanced to the highest values, nearly 100 and 100, 150 and 120, 350 and 300, and 1500 and 1200. An irregularity is also observed for electron concentration at time $\frac{t}{t_{tr}}$ = 0.1. As a result, with rising times and magnetic fields, there was a rise in the number density of charges at a lower recombination rate of $\beta' = 0.01$. Because electrons account for the majority of charge carriers in n-type semiconductors, their concentration is higher than that of holes.

Figures 4 and 5 show that the number density of charge carriers in the Langevin system was lower compared with the non-Langevin system due to a higher recombination rate with changing magnetic fields. As a result, the research revealed that the maximum electron concentration for an n-type doped semiconductor for $\beta' = 0.01$ in a non-Langevin system was approximately four times higher as compared with the Langevin system. Consequently, an increase in the dopant concentration from 1 to 3 increased the number density of charge carriers in the semiconductor.



(**a**) For $\beta' = 0.01$, $N_{p_d} = 3$ and $B'(z) = 0$

(**b**) For $\beta' = 0.01$, $N_{p_d} = 3$ and $B'(z) = 0.3$

(**c**) For $\beta' = 0.01$, $N_{p_d} = 3$ and $B'(z) = 0.6$

(**d**) For $\beta' = 0.01$, $N_{p_d} = 3$ and $B'(z) = 1$

Figure 5. Number density of electrons and holes varying with respect to position coordinate, magnetic field, and time for an n-type doped semiconductor with a dopant concentration of $N_{p_d} = 3$ in non-Langevin system $\beta' = 0.01$.

3.2. Effect of n-Type Doping on the Hall Voltage

Figures 6 and 7 indicate that numerical FEMs were used to calculate the Hall voltage as a function of the normalized position coordinate (y') for an n-type doped semiconductor at time $\frac{t}{t_{tr}} = 10$ for various magnetic fields by keeping x' constant at 0.5. The concentrations of dopant added to the semiconductor were 1 and 3. The data were examined for the recombination coefficients $\beta' = 1$ and 0.01 that, respectively, represent Langevin and non-Langevin recombinations between the charge carriers.

Figure 6a shows 0.49 as the lowest and highest voltage value for zero magnetic field at $\beta' = 1$, which represents Langevin recombination. For $B'(z) = 0.3, 0.6,$ and 1, the lowest and highest values of voltage observed were 0.40 and 0.59, 0.33 and 0.66, and 0.23 and 0.74, respectively, resulting in 0, 0.19, 0.33, and 0.51 as potential differences. Because the simulation had normalized equations, dimensionless values of Hall voltage were obtained. As a result, the Hall voltage increased along with the magnetic field for the dopant concentration of 1.

Figure 6b depicts for $\beta' = 0.01$, which represents non-Langevin recombination with a dopant concentration of 1, having the highest voltage values in descending order as 0.98, 0.84, 0.69, and 0.5, and the lowest voltage values in descending order as 0.01, 0.16, 0.31, and 0.5 for $B'(z)$ = 1, 0.6, 0.3, and 0, respectively. Descending potential differences resulting from these values were 0.97, 0.68, 0.38, and 0.

Figure 7a shows 0.47 as the lowest and highest voltage value for zero magnetic field at $\beta' = 1$, which defines Langevin recombination. For $B'(z) = 0.3, 0.6,$ and 1, the lowest and highest values of voltage observed were 0.39 and 0.59, 0.32 and 0.67, and 0.19 and 0.75, respectively, resulting in 0, 0.2, 0.35, and 0.56 as potential differences. Therefore, Hall voltage increased for a dopant concentration of 3 with an increasing magnetic field.

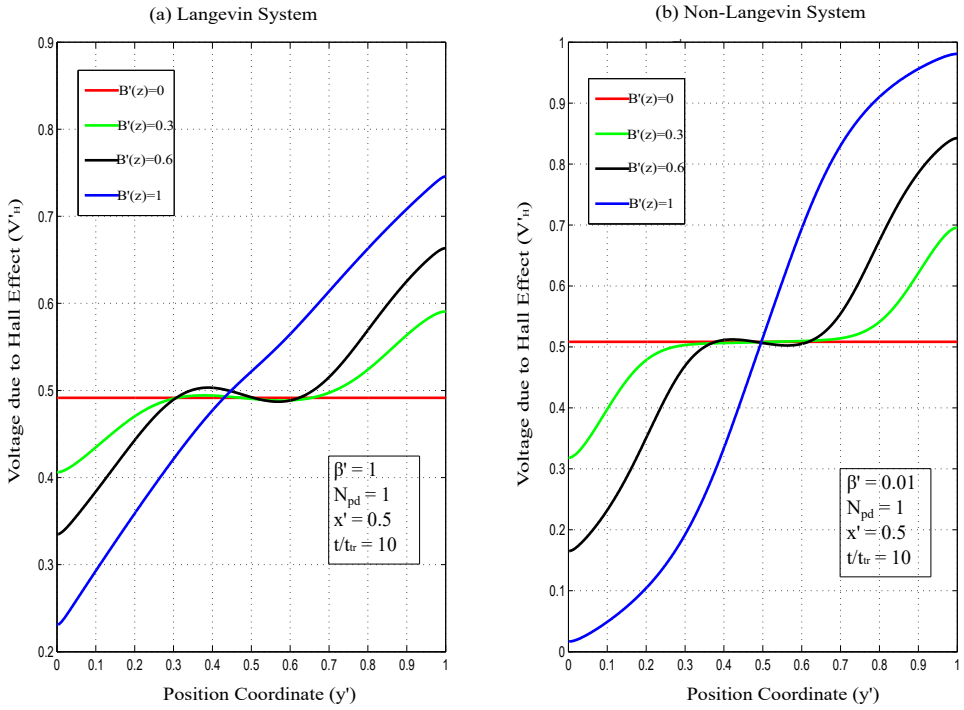


Figure 6. For an n-type doped semiconductor with a dopant concentration of $N_{p_d} = 1$ in Langevin $\beta' = 1$ (**a**) and non-Langevin $\beta' = 0.01$ (**b**) systems, Hall voltage varies with respect to position coordinate and magnetic field.

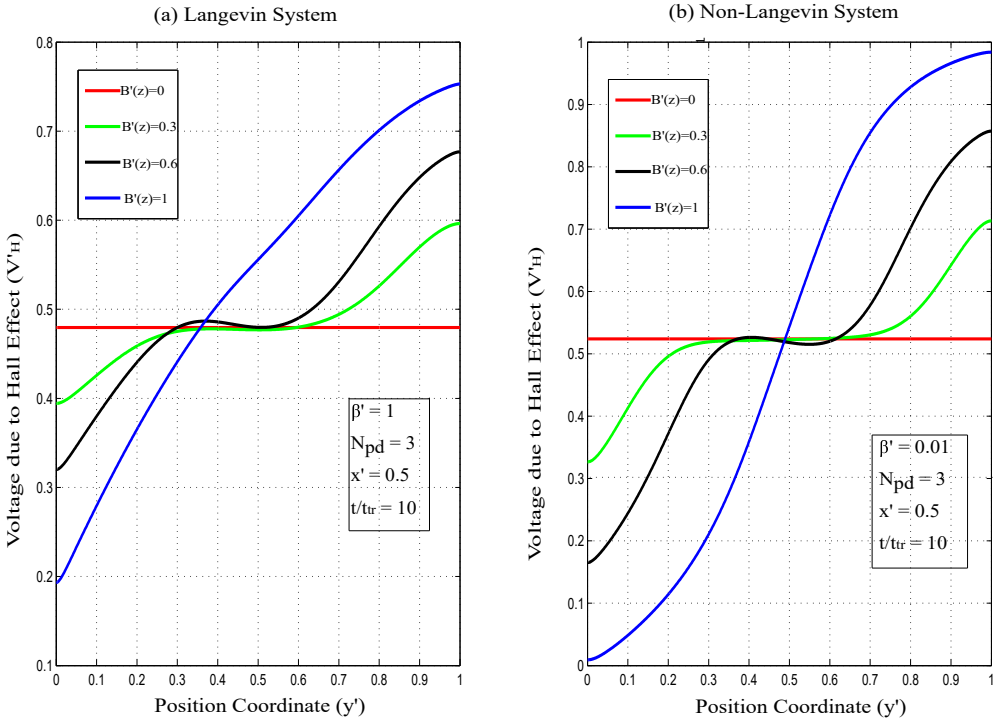


Figure 7. For an n-type doped semiconductor with a dopant concentration of $N_{p_d} = 3$ in Langevin $\beta' = 1$ (**a**) and non-Langevin $\beta' = 0.01$ (**b**) systems, Hall voltage varies with respect to position coordinate and magnetic field.

Figure 7b describes non-Langevin recombination with a dopant concentration of 3, having the highest voltage values in descending order as 0.98, 0.85, 0.71, and 0.52, and the lowest voltage values in descending order as 0.009, 0.16, 0.32, and 0.52, for $B'(z)$ = 1, 0.6, 0.3, and 0, respectively. Descending potential differences resulting from these values were

0.971, 0.69, 0.39, and 0. Consequently, these findings demonstrate that a rising magnetic field ascends the Hall voltage.

Figures 6 and 7 illustrate rising magnetic fields and dopant concentrations that advance the Hall voltage in an n-type doped semiconductor. Voltages obtained due to the Hall effect in steady-state and non-Langevin systems were higher compared with those in the Langevin system, as shown in Table 1. Moreover, Table 1 demonstrates identical Hall voltage values in steady-state and non-Langevin systems. $V_H = w\, B_z\, E_x\, \mu$ [65] defines the Hall voltage equation for steady-state. $V'_H = w'\, B'_z\, E'_x\, \mu'$ represents normalized equation that was employed in the simulation. Where w was semiconductor's width given by $w' = \frac{w}{d}$ and parameters w', E'_x, μ' have values of unity.

Table 1. Steady-state, non-Langevin, and Langevin systems showing Hall voltages (dimensionless quantity) in n-type doped semiconductor.

Magnetic Field $B'(z)$	**Langevin** $N_{p_d} = 1$	**Non-Langevin** $N_{p_d} = 1$	**Langevin** $N_{p_d} = 3$	**Non-Langevin** $N_{p_d} = 3$	**Steady State** V'_H
0	0	0	0	0	0
0.3	0.19	0.38	0.2	0.39	0.3
0.6	0.33	0.68	0.35	0.69	0.6
1	0.51	0.97	0.56	0.971	1

4. Conclusions

The number density of charge carriers can change significantly with varying magnetic fields, time, and the addition of dopants, which can cause modifications in the Hall voltage. Additionally, both non-Langevin and Langevin recombinations among charges have a significant impact on both the number density of charge carriers and Hall voltage. The findings of this research showed that the overall number density of charge carriers increases with an increase in dopant concentrations; however, as compared with non-Langevin systems of $\beta' = 0.01$, with increasing dopant concentrations of $N_{p_d} = 1$ and 3, the Langevin system of $\beta' = 1$ had the number density of charge carriers nearly five and four times lower, respectively, because of the high recombination rate between charges. Moreover, Langevin systems with different magnetic fields and dopant concentrations had lower Hall voltages than the steady-state and non-Langevin systems. While the non-Langevin system had nearly identical Hall voltages as the steady-state case. In conclusion, the significance of these findings provides new insights into improving device performance by understanding the notion of Hall effect and charge transport with dopants in organic semiconductors having low mobility. The number density of charge carriers and Hall voltages are important figures of merit that offer valuable insights into the electrical properties of organic semiconductors and are essential for optimizing the performance of electronic devices by improving their efficiency.

Author Contributions: Conceptualization, S.M. and A.P.; Methodology, S.M. and A.P.; Software, S.M.; Validation, S.M., M.M.S. and A.P.; Formal analysis, S.M.; Investigation, S.M.; Resources, M.M.S. and A.P.; Data curation, S.M.; Writing—original draft, S.M.; Writing—review & editing, S.M., M.M.S. and A.P.; Visualization, S.M.; Supervision, M.M.S. and A.P.; Project administration, S.M., M.M.S. and A.P.; Funding acquisition, M.M.S. and A.P. All authors have read and agreed to the published version of the manuscript.

Funding: This research was funded by the Murdoch University through an RTP scholarship granted by the Australian government.

Data Availability Statement: Data are contained within the article.

Acknowledgments: Computational resources were provided by the Murdoch University. S.M. acknowledges the financial support of the Australian Government Research Training Program Scholarship.

Conflicts of Interest: The authors declare no conflicts of interest.

References

1. Nishide, J.I.; Nakanotani, H.; Hiraga, Y.; Adachi, C. High-efficiency white organic light-emitting diodes using thermally activated delayed fluorescence. *Appl. Phys. Lett.* **2014**, *104*, 233304. [CrossRef]
2. Nakanotani, H.; Higuchi, T.; Furukawa, T.; Masui, K.; Morimoto, K.; Numata, M.; Tanaka, H.; Sagara, Y.; Yasuda, T.; Adachi, C. High-efficiency organic light-emitting diodes with fluorescent emitters. *Nat. Commun.* **2014**, *5*, 4016. [CrossRef]
3. Jou, J.H.; Kumar, S.; Agrawal, A.; Li, T.H.; Sahoo, S. Approaches for fabricating high efficiency organic light emitting diodes. *J. Mater. Chem. C* **2015**, *3*, 2974–3002. [CrossRef]
4. Miwa, T.; Kubo, S.; Shizu, K.; Komino, T.; Adachi, C.; Kaji, H. Blue organic light-emitting diodes realizing external quantum efficiency over 25% using thermally activated delayed fluorescence emitters. *Sci. Rep.* **2017**, *7*, 1–8. [CrossRef] [PubMed]
5. Lu, L.; Zheng, T.; Wu, Q.; Schneider, A.M.; Zhao, D.; Yu, L. Recent advances in bulk heterojunction polymer solar cells. *Chem. Rev.* **2015**, *115*, 12666–12731. [CrossRef]
6. Yuan, J.; Gu, J.; Shi, G.; Sun, J.; Wang, H.Q.; Ma, W. High efficiency all-polymer tandem solar cells. *Sci. Rep.* **2016**, *6*, 26459. [CrossRef]
7. Liu, J.; Chen, S.; Qian, D.; Gautam, B.; Yang, G.; Zhao, J.; Bergqvist, J.; Zhang, F.; Ma, W.; Ade, H.; et al. Fast charge separation in a non-fullerene organic solar cell with a small driving force. *Nat. Energy* **2016**, *1*, 16089. [CrossRef]
8. Youn, H.; Park, H.J.; Guo, L.J. Organic photovoltaic cells: From performance improvement to manufacturing processes. *Small* **2015**, *11*, 2228–2246. [CrossRef] [PubMed]
9. Fei, Z.; Pattanasattayavong, P.; Han, Y.; Schroeder, B.C.; Yan, F.; Kline, R.J.; Anthopoulos, T.D.; Heeney, M. Influence of side-chain regiochemistry on the transistor performance of high-mobility, all-donor polymers. *J. Am. Chem. Soc.* **2014**, *136*, 15154–15157. [CrossRef]
10. Bronstein, H.; Leem, D.S.; Hamilton, R.; Woebkenberg, P.; King, S.; Zhang, W.; Ashraf, R.S.; Heeney, M.; Anthopoulos, T.D.; Mello, J.d.; et al. Indacenodithiophene-co-benzothiadiazole copolymers for high performance solar cells or transistors via alkyl chain optimization. *Macromolecules* **2011**, *44*, 6649–6652. [CrossRef]
11. Zhang, X.; Bronstein, H.; Kronemeijer, A.J.; Smith, J.; Kim, Y.; Kline, R.J.; Richter, L.J.; Anthopoulos, T.D.; Sirringhaus, H.; Song, K.; et al. Molecular origin of high field-effect mobility in an indacenodithiophene–benzothiadiazole copolymer. *Nat. Commun.* **2013**, *4*, 2238. [CrossRef]
12. Yan, H.; Chen, Z.; Zheng, Y.; Newman, C.; Quinn, J.R.; Dötz, F.; Kastler, M.; Facchetti, A. A high-mobility electron-transporting polymer for printed transistors. *Nature* **2009**, *457*, 679–686. [CrossRef] [PubMed]
13. Paterson, A.F.; Singh, S.; Fallon, K.J.; Hodsden, T.; Han, Y.; Schroeder, B.C.; Bronstein, H.; Heeney, M.; McCulloch, I.; Anthopoulos, T.D. Recent progress in high-mobility organic transistors: A reality check. *Adv. Mater.* **2018**, *30*, 1801079. [CrossRef] [PubMed]
14. Uemura, T.; Rolin, C.; Ke, T.H.; Fesenko, P.; Genoe, J.; Heremans, P.; Takeya, J. On the Extraction of Charge Carrier Mobility in High-Mobility Organic Transistors. *Adv. Mater.* **2016**, *28*, 151–155. [CrossRef]
15. Mandal, S.; Noh, Y.Y. Printed organic thin-film transistor-based integrated circuits. *Semicond. Sci. Technol.* **2015**, *30*, 064003. [CrossRef]
16. Lee, T.; Chen, Y. Organic resistive nonvolatile memory materials. *MRS Bull.* **2012**, *37*, 144–149. [CrossRef]
17. Yamamoto, Y.; Yoshino, K.; Inuishi, Y. Electrical properties of phthalocyanine-halogen complexes. *J. Phys. Soc. Jpn.* **1979**, *47*, 1887–1891. [CrossRef]
18. Chiang, C.K.; Fincher, C., Jr.; Park, Y.W.; Heeger, A.J.; Shirakawa, H.; Louis, E.J.; Gau, S.C.; MacDiarmid, A.G. Electrical conductivity in doped polyacetylene. *Phys. Rev. Lett.* **1977**, *39*, 1098. [CrossRef]
19. McNeill, R.; Siudak, R.; Wardlaw, J.; Weiss, D. Electronic conduction in polymers. I. The chemical structure of polypyrrole. *Aust. J. Chem.* **1963**, *16*, 1056–1075. [CrossRef]
20. De Surville, R.; Jozefowicz, M.; Yu, L.; Pepichon, J.; Buvet, R. Electrochemical chains using protolytic organic semiconductors. *Electrochim. Acta* **1968**, *13*, 1451–1458. [CrossRef]
21. McGinness, J.; Corry, P.; Proctor, P. Amorphous semiconductor switching in melanins. *Science* **1974**, *183*, 853–855. [CrossRef] [PubMed]
22. Parthasarathy, G.; Shen, C.; Kahn, A.; Forrest, S. Lithium doping of semiconducting organic charge transport materials. *J. Appl. Phys.* **2001**, *89*, 4986–4992. [CrossRef]
23. Kido, J.; Matsumoto, T. Bright organic electroluminescent devices having a metal-doped electron-injecting layer. *Appl. Phys. Lett* **1998**, *73*, 2866. [CrossRef]
24. Endo, J.; Matsumoto, T.; Kido, J. Organic electroluminescent devices with a vacuum-deposited Lewis-acid-doped hole-injecting layer. *Jpn. J. Appl. Phys.* **2002**, *41*, L358. [CrossRef]
25. Kearns, D.R.; Tollin, G.; Calvin, M. Electrical properties of organic solids. II. effects of added electron acceptor on metal-free phthalocyanine. *J. Chem. Phys.* **1960**, *32*, 1020–1025. [CrossRef]
26. Maitrot, M.; Guillaud, G.; Boudjema, B.; André, J.; Simon, J. Molecular material-based junctions: Formation of a Schottky contact with metallophthalocyanine thin films doped by the cosublimation method. *J. Appl. Phys.* **1986**, *60*, 2396–2400. [CrossRef]
27. Andre, J.; Simon, J.; Even, R.; Boudjema, B.; Guillaud, G.; Maitrot, M. Molecular semiconductors and junction formation: Phthalocyanine derivatives. *Synth. Met.* **1987**, *18*, 683–688. [CrossRef]
28. Marks, T.J. Electrically conductive metallomacrocyclic assemblies. *Science* **1985**, *227*, 881–889. [CrossRef]

29. Lous, E.; Blom, P.; Molenkamp, L.; De Leeuw, D. Schottky contacts on a highly doped organic semiconductor. *Phys. Rev. B* **1995**, *51*, 17251. [CrossRef]
30. Maennig, B.; Pfeiffer, M.; Nollau, A.; Zhou, X.; Leo, K.; Simon, P. Controlled p-type doping of polycrystalline and amorphous organic layers: Self-consistent description of conductivity and field-effect mobility by a microscopic percolation model. *Phys. Rev. B* **2001**, *64*, 195208. [CrossRef]
31. Harada, K.; Werner, A.; Pfeiffer, M.; Bloom, C.; Elliott, C.; Leo, K. Organic homojunction diodes with a high built-in potential: Interpretation of the current-voltage characteristics by a generalized Einstein relation. *Phys. Rev. Lett.* **2005**, *94*, 036601. [CrossRef] [PubMed]
32. Olthof, S.; Tress, W.; Meerheim, R.; Lüssem, B.; Leo, K. Photoelectron spectroscopy study of systematically varied doping concentrations in an organic semiconductor layer using a molecular p-dopant. *J. Appl. Phys.* **2009**, *106*, 103711. [CrossRef]
33. Huang, Q.; Walzer, K.; Pfeiffer, M.; Lyssenko, V.; He, G.; Leo, K. Highly efficient top emitting organic light-emitting diodes with organic outcoupling enhancement layers. *Appl. Phys. Lett.* **2006**, *88*, 113515. [CrossRef]
34. Meerheim, R.; Walzer, K.; Pfeiffer, M.; Leo, K. Ultrastable and efficient red organic light emitting diodes with doped transport layers. *Appl. Phys. Lett.* **2006**, *89*, 061111. [CrossRef]
35. Reineke, S.; Lindner, F.; Schwartz, G.; Seidler, N.; Walzer, K.; Lüssem, B.; Leo, K. White organic light-emitting diodes with fluorescent tube efficiency. *Nature* **2009**, *459*, 234–238. [CrossRef]
36. Schulze, K.; Uhrich, C.; Schüppel, R.; Leo, K.; Pfeiffer, M.; Brier, E.; Reinold, E.; Bäuerle, P. Efficient vacuum-deposited organic solar cells based on a new low-bandgap oligothiophene and fullerene C60. *Adv. Mater.* **2006**, *18*, 2872–2875. [CrossRef]
37. Uhrich, C.; Wynands, D.; Olthof, S.; Riede, M.K.; Leo, K.; Sonntag, S.; Maennig, B.; Pfeiffer, M. Origin of open circuit voltage in planar and bulk heterojunction organic thin-film photovoltaics depending on doped transport layers. *J. Appl. Phys.* **2008**, *104*, 043107. [CrossRef]
38. Wynands, D.; Levichkova, M.; Leo, K.; Uhrich, C.; Schwartz, G.; Hildebrandt, D.; Pfeiffer, M.; Riede, M. Increase in internal quantum efficiency in small molecular oligothiophene: C 60 mixed heterojunction solar cells by substrate heating. *Appl. Phys. Lett.* **2010**, *97*, 073503. [CrossRef]
39. Fallahpour, A.; Gagliardi, A.; Gentilini, D.; Zampetti, A.; Santoni, F.; Auf der Maur, M.; Di Carlo, A. Optoelectronic simulation and thickness optimization of energetically disordered organic solar cells. *J. Comput. Electron.* **2014**, *13*, 933–942. [CrossRef]
40. Gagliardi, A.; der Maur, M.A.; Gentilini, D.; di Fonzo, F.; Abrusci, A.; Snaith, H.J.; Divitini, G.; Ducati, C.; Di Carlo, A. The real TiO 2/HTM interface of solid-state dye solar cells: Role of trapped states from a multiscale modelling perspective. *Nanoscale* **2015**, *7*, 1136–1144. [CrossRef]
41. Fallahpour, A.H.; Gentilini, D.; Gagliardi, A.; der Maur, M.A.; Lugli, P.; Di Carlo, A. Systematic study of the PCE and device operation of organic tandem solar cells. *IEEE J. Photovoltaics* **2015**, *6*, 202–210. [CrossRef]
42. Darwish, M.; Boysan, H.; Liewald, C.; Nickel, B.; Gagliardi, A. A resistor network simulation model for laser-scanning photo-current microscopy to quantify low conductance regions in organic thin films. *Org. Electron.* **2018**, *62*, 474–480. [CrossRef]
43. Gagliardi, A.; Wang, S.; Albes, T. Simulation of charge Carrier mobility unbalance in organic solar cells. *Org. Electron.* **2018**, *59*, 171–176. [CrossRef]
44. Zubair, M.; Ang, Y.S.; Ang, L.K. Thickness dependence of space-charge-limited current in spatially disordered organic semiconductors. *IEEE Trans. Electron Devices* **2018**, *65*, 3421–3429. [CrossRef]
45. Pivrikas, A.; Neugebauer, H.; Sariciftci, N.S. Charge carrier lifetime and recombination in bulk heterojunction solar cells. *IEEE J. Sel. Top. Quantum Electron.* **2010**, *16*, 1746–1758. [CrossRef]
46. Pivrikas, A.; Ullah, M.; Simbrunner, C.; Sitter, H.; Neugebauer, H.; Sariciftci, N.S. Comparative study of bulk and interface transport in disordered fullerene films. *Phys. Status Solidi (B)* **2011**, *248*, 2656–2659. [CrossRef]
47. Funahashi, M. Time-of-Flight Method for Determining the Drift Mobility in Organic Semiconductors. In *Organic Semiconductors for Optoelectronics*; Wiley: Hoboken, NJ, USA, 2021; pp. 161–178.
48. Yi, H.; Gartstein, Y.N.; Podzorov, V. Charge carrier coherence and Hall effect in organic semiconductors. *Sci. Rep.* **2016**, *6*, 23650. [CrossRef] [PubMed]
49. Choi, H.H.; Paterson, A.F.; Fusella, M.A.; Panidi, J.; Solomeshch, O.; Tessler, N.; Heeney, M.; Cho, K.; Anthopoulos, T.D.; Rand, B.P.; et al. Hall effect in polycrystalline organic semiconductors: The effect of grain boundaries. *Adv. Funct. Mater.* **2020**, *30*, 1903617. [CrossRef]
50. Neukom, M.; Reinke, N.; Ruhstaller, B. Charge extraction with linearly increasing voltage: A numerical model for parameter extraction. *Solar Energy* **2011**, *85*, 1250–1256. [CrossRef]
51. Koster, L.J.; Smits, E.; Mihailetchi, V.; Blom, P.W. Device model for the operation of polymer/fullerene bulk heterojunction solar cells. *Phys. Rev. B* **2005**, *72*, 085205. [CrossRef]
52. Hwang, I.; McNeill, C.R.; Greenham, N.C. Drift-diffusion modeling of photocurrent transients in bulk heterojunction solar cells. *J. Appl. Phys.* **2009**, *106*, 094506. [CrossRef]
53. Neukom, M.T.; Züfle, S.; Ruhstaller, B. Reliable extraction of organic solar cell parameters by combining steady-state and transient techniques. *Org. Electron.* **2012**, *13*, 2910–2916. [CrossRef]
54. MacKenzie, R.C.; Shuttle, C.G.; Chabinyc, M.L.; Nelson, J. Extracting microscopic device parameters from transient photocurrent measurements of P3HT: PCBM solar cells. *Adv. Energy Mater.* **2012**, *2*, 662–669. [CrossRef]

55. Hanfland, R.; Fischer, M.A.; Brütting, W.; Würfel, U.; MacKenzie, R.C. The physical meaning of charge extraction by linearly increasing voltage transients from organic solar cells. *Appl. Phys. Lett.* **2013**, *103*, 063904. [CrossRef]
56. Hwang, I.; Greenham, N.C. Modeling photocurrent transients in organic solar cells. *Nanotechnology* **2008**, *19*, 424012. [CrossRef]
57. Rogel-Salazar, J.; Bradley, D.D.; Cash, J.; Demello, J. An efficient method-of-lines simulation procedure for organic semiconductor devices. *Phys. Chem. Chem. Phys.* **2009**, *11*, 1636–1646. [CrossRef]
58. Juška, G.; Viliunas, M.; Klíma, O.; Šípek, E.; Kočka, J. New features in space-charge-limited-photocurrent transients. *Philos. Mag. B* **1994**, *69*, 277–289. [CrossRef]
59. Juška, G.; Viliunas, M.; Arlauskas, K.; Kočka, J. Space-charge-limited photocurrent transients: The influence of bimolecular recombination. *Phys. Rev. B* **1995**, *51*, 16668. [CrossRef]
60. Pivrikas, A.; Juška, G.; Mozer, A.J.; Scharber, M.; Arlauskas, K.; Sariciftci, N.; Stubb, H.; Österbacka, R. Bimolecular recombination coefficient as a sensitive testing parameter for low-mobility solar-cell materials. *Phys. Rev. Lett.* **2005**, *94*, 176806. [CrossRef]
61. Pivrikas, A.; Sariciftci, N.S.; Juška, G.; Österbacka, R. A review of charge transport and recombination in polymer/fullerene organic solar cells. *Prog. Photovoltaics Res. Appl.* **2007**, *15*, 677–696. [CrossRef]
62. Blochwitz, J.; Fritz, T.; Pfeiffer, M.; Leo, K.; Alloway, D.M.; Lee, P.A.; Armstrong, N.R. Interface electronic structure of organic semiconductors with controlled doping levels. *Org. Electron.* **2001**, *2*, 97. [CrossRef]
63. Werner, A.; Li, F.; Harada, K.; Pfeiffer, M.; Fritz, T.; Leo, K.; Machill, S. n-Type doping of organic thin films using cationic dyes. *Adv. Funct. Mater.* **2004**, *14*, 255–260. [CrossRef]
64. Li, F.; Werner, A.; Pfeiffer, M.; Leo, K.; Liu, X. Leuco crystal violet as a dopant for n-doping of organic thin films of fullerene C60. *J. Phys. Chem. B* **2004**, *108*, 17076–17082. [CrossRef]
65. Ellmer, K. Hall effect and conductivity measurements in semiconductor crystals and thin films. In *Characterization of Materials*; Wiley: Hoboken, NJ, USA, 2012; pp. 1–16.

Disclaimer/Publisher's Note: The statements, opinions and data contained in all publications are solely those of the individual author(s) and contributor(s) and not of MDPI and/or the editor(s). MDPI and/or the editor(s) disclaim responsibility for any injury to people or property resulting from any ideas, methods, instructions or products referred to in the content.